RESEARCH ARTICLE
doi: 10.2306/scienceasia1513-1874.2025.s023

ScienceAsia 51S (2): 2025: ID 2025s023: **1–9**

Investigation of oxygen evolution reaction using a co-doped Ir/Sb-SnO_2 as electrocatalytic electrode materials

Supandee Maneelok[a,*], **Chakkrapong Chaiburi**[b], **Chontira Sangsubun**[c], **Pierrot S. Attidekou**[d]

[a] Department of Occupational Health and Safety, Faculty of Health and Sports Science, Thaksin University, Phatthalung 93210 Thailand
[b] Faculty of Engineering, Thaksin University, Phatthalung Campus, Phatthalung 93210 Thailand
[c] Department of Physical Sciences, Faculty of Science and Digital Innovation, Thaksin University, Phatthalung 93210 Thailand
[d] School of Chemistry, University of Birmingham, Birmingham B15 2TT United Kingdom

*Corresponding author, e-mail: msupandee@tsu.ac.th

Received 30 Nov 2024, Accepted 20 Oct 2025
Available online 20 Dec 2025

ABSTRACT: Iridium antimony-doped tin oxide (Ir/ATO) is a promising catalytic material for the anodic oxygen evolution reaction (OER), a significant challenge in clean energy technologies such as energy storage, energy conversion, and electrolysis. In this study, Ti/Ir/ATO electrodes were fabricated using the dip coating method with various Ir concentrations at different calcination temperatures. The oxygen evolution reaction was evaluated. The material properties were characterized by X-ray diffraction (XRD), scanning electron microscope (SEM), Energy-dispersive X-ray spectroscopy (EDX), X-ray photoelectron spectroscopy (XPS), and Cyclic voltammetry (CV). The Ir/ATO materials exhibit a single-phase tetragonal structure with nano-sized particles ranging from 8.2 to 24 nm as a function of doping at 550 °C. The spherical particles and EDX mapping show uniformly distributed Ir and Sb atoms over tin oxide with no aggregation. XPS spectra of Ir/ATO calcined at 550 °C showed the presence of Sn^{4+} and both Sb^{3+} and Sb^{5+}. The highest Sb^{3+} peak area of 2.5% Ir/ATO suggests enhanced kinetics due to substitution and increased number of electrochemically active sites. With regard to OER performance, the CV performed on a 2.5%Ir/ATO catalyst exhibits a cathodic surface oxide reduction peak around ca. 0.47 V (vs. Ag/AgCl) with a current density of 2.03 mA cm^{-2} and a surface oxidation onset around E = 0.8V. Furthermore, an onset potential for the OER can be observed at ca. 1.4 V, indicating superior OER properties.

KEYWORDS: electrochemical catalyst, oxygen evolution reaction, iridium antimony-doped tin oxide, electrocatalyst

INTRODUCTION

Electrochemistry, as the investigation of the oxygen evolution reaction (OER) in the water splitting process, has gained widespread attention because it can produce hydrogen and oxygen, which are applied in energy-related technologies such as energy storage, energy conversion, and clean energy technologies. These include hydrogen production, renewable energy storage, metal-air batteries, and fuel cells [1–4]. The OER is a water oxidation process that produces oxygen molecules and four protons, with an equilibrium half-cell potential of 1.23 V in an acidic solution [2–5]. However, the thermodynamics and kinetics processes of the OER indicate that the reaction involves multiple steps of proton movement to form oxygen molecules. The cumulative energy from each step results in a slowdown of the electrochemical reaction kinetics, requiring a higher applied potential [2]. To address this issue, the most efficient materials as catalysts have been investigated to improve the efficiency of OER.

Extensive studies have been conducted on electrode materials for OER, including transition metals such as Co, Ir, Ru, Nb, Ni, Fe, and others [6], and compounds corresponding to hydroxides, sulfides, oxides, etc. [4, 7–9]. Additionally, metal oxide catalysts such as tin oxide (SnO_2) and manganese oxide (MnO) have been studied for electrode structure. It was found that both metal oxides have low electrical conductivity [8]. However, their conductivity can be improved by doping with transition metals. Therefore, the transition metal antimony (Sb) has been selected as a dopant in tin oxide, resulting in Sb-SnO_2 (ATO), and this material has been employed as a catalyst to enhance oxygen evolution reaction and optimize the electrocatalyst properties [10]. Further improvements have been made to Sb-SnO_2 by doping it with noble metals such as Ir, Ru, Pd, Au, Nb, Ti, and Ta [2, 11, 12]. Oh et al [13] studied the reaction of IrO_x with ATO nanoparticles to enhance OER efficiency and found that ATO is a suitable support material for Ir particles, which provides improved stability in acidic solutions. This finding is consistent with studies by Chen et al [14] and Perez et al [10], which showed that Ti/IrO_x-Sb_2O_5-SnO_2 electrodes are highly stable and have suitable conductivity for the OER. Regarding using metal alloys to enhance OER efficiency, the reaction of the electrocatalyst can be explained by the adsorption energies of intermediates that occur in the intrinsic activity or the number of active sites on the catalyst. Kim et al [15] and Xu et al [16] explained the increase in intrinsic activity at the active sites on the

catalyst surface by stating that the adsorption energy at these sites can be affected when another metal is substituted, resulting in increased electrical conductivity of the catalyst. In principle, the adsorption energy of intermediates on the catalyst surface can be determined from the electronic structure. In highly conductive catalysts, the metal valence states lie in the d-band, and the oxygen valence states lie in the p-band, both near the Fermi level, which is used to calculate the adsorption energy of the metal [13].

As mentioned earlier, the efficiency of mixed catalysts for OER also depends on the synthesis method. There are various synthesis methods such as chlorine-free Adams fusion [16, 17], the soft-template method and colloidal method [4], the coating method [18], and the thermal method [10]. It is evident that all these synthesis methods help increase the surface area for the reaction at the active sites of the catalyst. As a result, nanoparticles have been considered a key factor in catalyst preparation due to their high surface area and conductivity [22–25]. Therefore, the size of the metal oxide particles depends on the preparation method and calcination temperature. A simple synthesis method that can enhance the catalytic efficiency of the electrocatalyst is the coating method, which enables both heterogeneous and homogeneous catalysts to adhere to the surface of the anode [19].

With respect to the effect of calcination temperature, it was found to impact the electronic structure of the catalyst, with higher conductivity at higher calcination temperatures [7, 20]. Studies on the effect of calcination temperature on IrO_2, Ir-IrO_2, Ti/IrO_2-Sb_2O_5-SnO_2, and Ir/ATO anodes showed that the optimal calcination temperature range for achieving high stability and activity in the anodes is between 500–800 °C [5, 14, 16, 17]. In addition, the chemical composition of alloy-based catalysts is also crucial, as doping with different metals affects the shape, oxidation state, and surface area of the catalyst. Thus, metal alloys represent another strategy to enhance OER performance. The electronic structure of the host phase can be modified by doping, with transition metals replacing other atoms in the crystal structure, leading to increased adsorption energy and improved reaction kinetics for OER [4].

Therefore, this research focuses on the effect of dopants on antimony-doped tin oxide electrodes on the efficiency of electrocatalysts for the oxygen evolution reaction. Iridium (Ir) was selected as a dopant, and the effects of dopant concentration and calcination temperature on the performance of Ti/Ir/ATO electrodes for OER were investigated.

MATERIALS AND METHODS

Materials

Chemicals and reagents employed in this synthesis were Tin (IV) chloride pentahydrate, ($SnCl_4 \cdot 5\,H_2O$) (98%, Sigma-Aldrich, St. Louis, MO, USA), Antimony trichloride ($SbCl_3$) (99%, Sigma-Aldrich), and Iridium (III) chloride hydrate ($IrCl_3 \cdot xH_2O$) (99.9%, Sigma-Aldrich), used as received. The ethanol (C_2H_5OH, AR > 99.9%) and acetone (C_3H_6O, AR > 99.9%) were purchased from Merck (Darmstadt, Germany).

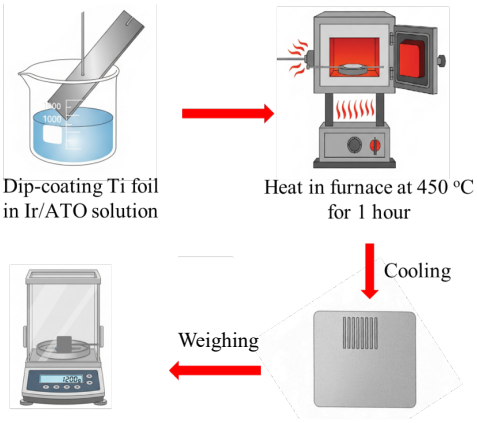

Fig. 1 Schematic of Ti/Ir/ATO electrode preparation.

Synthesis of mixed oxide catalysts

The Ir/ATO anodes were prepared using the dip-coating method. The anode preparation steps were adapted from the method of Maneelok and Attidekou [21]. A titanium substrate of 0.8 × 0.8 cm was employed. The precursor solutions for Ir/ATO were prepared from $SnCl_4 \cdot 5\,H_2O$, $SbCl_3$, and $IrCl_3 \cdot xH_2O$ in molar ratios Sn:Sb:Ir of 500:8:x, respectively, where x represents Ir at concentrations of 0.5, 1, 1.5, 2, and 2.5. The preparation method was adapted from the work of Maneelok and Attidekou [21] and Perez-Viramontes et al [10]. The Ti/Ir/ATO anodes were fabricated by creating thin films on the surface of the substrate (Ti) using the dip-coating method. The prepared electrodes were dipped into the Ir/ATO precursor solution and then calcined in a furnace at 450 °C. This dip-coating and calcined process was repeated, with the final calcining step lasting for 1 h. Then, the electrodes were allowed to cool to room temperature, as shown in Fig. 1. This study examined the effect of calcination temperature on the OER, with electrodes fabricated at 500 and 550 °C.

Characterization techniques

X-ray diffraction (XRD) measurements were conducted using a Panalytical EMPYREAN powder diffractometer (Malvern, UK) equipped with Cu-Kα radiation (λ = 1.5406 Å) at operating conditions of 40 kV and 40 mA. The morphology of the synthesized materials was examined via field emission scanning electron microscopy (FESEM) (FEI Quanta450 FEG model, 5 kV, Oregon, USA) working at an accelerating voltage of 200 kV. The chemical composition of the prepared

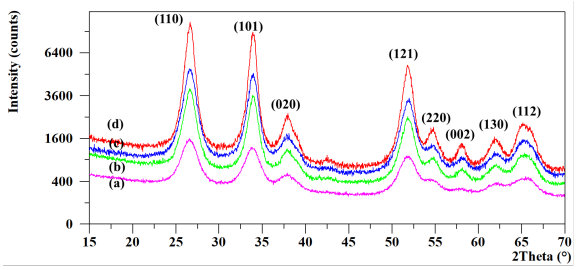

Fig. 2 The XRD patterns of the Ir/ATO catalyst calcined at 550 °C with various Ir contents at (a) 0.5 mol%, (b) 1 mol%, (c) 2 mol%, and (d) 2.5 mol%.

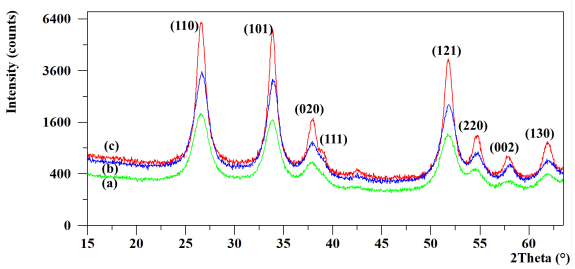

Fig. 3 The XRD patterns of the Ir/ATO catalyst with the 2% of Ir content at varying calcined temperatures at (a) 450 °C, (b) 500 °C, and (c) 550 °C.

Table 1 A variation of lattice parameters and crystallite size.

Sample	Calcined temp. (°C)	a (nm)	c (nm)	Crystallite size (nm)
ATO	450	4.7372	3.1841	7.2
ATO	500	4.7390	3.1826	8.9
ATO	550	4.7396	3.1819	10.8
0.5% Ir/ATO	550	4.7397	3.1851	12.1
1% Ir/ATO	550	4.7398	3.1858	14.6
1.5% Ir/ATO	550	4.7401	3.1862	17.5
2% Ir/ATO	450	4.7398	3.1851	18.4
2% Ir/ATO	500	4.7401	3.1856	19.2
2% Ir/ATO	550	4.7402	3.1865	20.3
2.5% Ir/ATO	550	4.7402	3.1864	24.4

materials was analyzed using the FESEM equipped with an Energy-dispersive X-ray (EDX) detector (X-Max50, Oxford Instrument, Abingdon, UK). X-ray photoelectron spectroscopy (XPS) (Thermo K-alpha, Hillsboro, Oregon, USA) with 72 W monochromated Al-Kα radiation (photon energy of 1486.6 eV) was used to evaluate elemental composition. The XPSpeak41 program was employed for peak fitting. The binding energy of the C1s peak at 284.6 eV was used as a reference to correct the peak shift.

Electrochemical characterization

Cyclic voltammograms (CVs) were recorded within a potential range of 0 V to 1.4 V (vs. Ag/AgCl) at a scan rate of 50 mV/s in an argon-saturated 0.5 M H_2SO_4 solution. For the OER, steady-state polarization curves were obtained in an oxygen-saturated electrolyte solution at a scan rate of 5 mV/s.

RESULTS AND DISCUSSION

X-ray diffraction analysis

The XRD technique was employed to analyze the structure of ATO thin films synthesized at calcination temperatures of 450, 500, and 550 °C and revealed that all samples exhibited X-ray diffraction patterns at the same positions on the planes (110), (101), (020), (121), (220), (002), (130), and (112), which correspond to the tetragonal crystal structure of SnO_2, according to the standard data for cassiterite, syn; Q: S; 00-041-1445, using Space group: P42/mnm. The Sb-SnO_2 structure is single phase, with no contamination from other compounds. Doping Sb into SnO_2 affects the physicochemical properties of SnO_2, where Sb enters the SnO_2 lattice and integrates uniformly, maintaining the single crystal structure of cassiterite. Based on ionic radius size consideration, Sn in SnO_2 (i.e., Sn^{4+} with a radius of 0.83 Å) can be easily substituted by Sb, which has a smaller ionic radius either in the form of Sb^{3+} (0.76 Å) or Sb^{5+} (0.62 Å) [22]. Overall, an ion with a smaller radius can replace its bigger counterpart, and the ionic radii in ATO can be classified in size as follows: $Sn^{4+} > Sb^{3+} > Sb^{5+}$. The XRD patterns of the Ti/Ir/ATO anodes calcined at 550 °C, with Ir doping concentrations of 0.5%, 1%, 2%, and 2.5% by mol, shown in Fig. 2, reveal that all XRD patterns of all Ir contents investigated are isostructural and exhibit a single crystal structure with no contamination from other compounds, even with Ir doping as high as 2.5% [20]. However, at a fixed temperature of 550 °C, a variation of lattice parameters is observed in both "a" and "c" with the ratio $c/a < 0$. Additionally, the lattice parameters "a" and "c" increase with Ir content up to 2 mol% and then remain nearly constant between 2 and 2.5 mol%, depicting the effect of concentration as shown in Table 1. The ionic radius for Ir cations is smaller than the Sn ionic radius in SnO_2 and therefore can replace its bigger counterpart, justifying the possibility of Ir insertion into the crystal structure. Alternatively, at fixed concentration (i.e., 2 mol% Ir content), both lattice parameters "a" and "c" increase with increasing temperature from 450 °C to 550 °C, and this is probably due to thermal expansion. The result is similar to the study on the structure of iridium oxide for oxygen synthesis by Abbott et al [17], who reported that iridium oxide calcined at temperatures higher than 500 °C exhibits a single rutile crystal structure. It was also reported that the ionic radii of Sn^{4+} (0.83 Å) and Ir^{4+} (0.77 Å) allow Ir^{4+} to replace Sn^{4+} ions, resulting in a single structure [14]. Additionally, Chen et al [14] and Oh et al [13] reported 2θ values for Ir-ATO of 740.7°, 47.3°, 69.1°, 83.4°, 88°, and 121.9°, with the

2θ at 40.7° representing the (111) plane according to JCPDS card no. 87-0715 [13]. Furthermore, it can be seen in Fig. 2 and Fig. 3 that the (111) plane at 2θ of 39.7° is becoming more discernible with an increase in Ir content and an increase in temperature. This indicates that Ir has replaced Sn in the crystal structure of ATO. Regarding the effect of Ir doping on crystallite size, calculated using the Scherrer equation, for the samples calcined at 550 °C, it is clear that the addition of Ir causes an increase in crystallite size from 12.1 nm for 0.5 mol% Ir to 24.4 nm for 2.5 mol% Ir.

The effects of calcination temperatures between 450 °C and 550 °C on Ir/ATO with an Ir doping concentration of 2 mol% were investigated. The results of this study indicate that calcination temperatures from 450 °C to 550 °C in Fig. 3 do not affect the structure of Ir/ATO. As the calcination temperature increases, the full width at half maximum (FWHM) decreases, indicating that the Ir/ATO catalyst becomes more crystalline, as shown by the peaks at the (110), (101), and (121) planes [17]. Additionally, the crystallite size increases with both temperature and Ir content. With respect to the crystallite size of 2% Ir/ATO, the calculated average crystallite size is from 18.4 nm to 20.3 nm at calcination temperatures from 450 °C to 550 °C, suggesting that the Ir dopant could affect the growth of the crystallite size.

Scanning electron microscopy and energy-dispersive X-ray spectroscopy analysis

Fig. 4 shows SEM images of the Ir/ATO electrodes synthesized at a calcination temperature of 550 °C with Ir doping concentrations of (a) 0.5%, (b) 1%, (c) 2%, and (d) 2.5% by mol. With respect to the morphology of Ir/ATO particles, a spherical particle shape was observed independently of doping levels [14]. The approximate particle sizes at Ir doping concentrations of 0.5%, 1%, 2%, and 2.5% were ca. 36 nm, 38 nm, 41 nm, and 44 nm, respectively. With respect to the chemical composition analysis, the EDX technique (Fig. 5) revealed the main detected elements, including Sn, Sb, Ir, and O. Despite the low doping level, Ir was detected. Furthermore, EDX Mapping confirmed the presence of Ir in the Ir/ATO catalyst. Fig. 6 shows the EDX mapping images of the Ir/ATO anode electrodes synthesized at a calcination temperature of 550 °C with Ir doping concentrations of 0.5% and 2.5% by mol. The elements Sn, Sb, and Ir were well-dispersed with no agglomeration throughout the samples. Fig. 6 has consistently exhibited the elemental distribution of the cations (Sn, Sb, Ir) throughout the samples, confirming their presence in the Ir/ATO catalyst. This result confirms that Ir was successfully incorporated into the Ir/ATO catalyst. The composition of Sn, Sb, and Ir in the Ir/ATO synthesized materials showed the mass concentration of Sn, Sb, and O of ca. 65 wt%, 5.6 wt%, and 32 wt%, respectively. The Ir mass concentrations were 0.26, 0.21, 0.29, and 0.28 wt% for 0.5%Ir/ATO to 2.5%Ir/ATO. The analysis revealed that the experimentally measured elemental percentages deviated from the nominal values calculated during preparation. Such variations are often inherent to the EDX technique, as the measured composition is sensitive to the spatial distribution of the catalyst particles, which can result in values lower than the theoretical loading.

X-ray photoelectron spectroscopy analysis

With respect to the oxidation state of elements, the photoelectron peaks of Sn and Sb in ATO crystals calcined at 550 °C are shown in Fig. 7. The photoelectron peaks analyzed correspond to Sn3d, Sb3d, and O1s at specific electron binding energies. The photoelectron peaks for $Sn3d_{3/2}$ and $Sn3d_{5/2}$ were observed at binding energies of 495.40–495.68 eV and 487.05–487.28 eV, respectively. The difference between the $Sn3d_{3/2}$ and $Sn3d_{5/2}$ peaks was approximately 8.4 eV, indicating that the binding energy corresponds to the oxidation state of Sn^{4+}. Regarding the photoelectron peaks for $Sb3d_{3/2}$ and $Sb3d_{5/2}$, it was found that the $Sb3d_{5/2}$ peak showed an overlap of the electron binding energies of both Sb and O, as shown in Fig. 7. Therefore, the $Sb3d_{3/2}$ peak was used for analysis. The binding energies were 540.05–540.25 eV and 540.80–540.97 eV, corresponding to the oxidation states of Sb^{3+} and Sb^{5+}, respectively. Thus, the oxidation states of the elements in the ATO crystal are Sn^{4+}, Sb^{3+}, and Sb^{5+}.

Moreover, for Ir/ATO (Fig. 7), no Ir4f peaks were detected in the binding energy region of 60–65 eV, which may be attributed to the lower Ir doping level. The peaks related to Ir were expected around 60.79, 61.76, and 62.43 eV corresponding to Ir^0 $4f_{7/2}$, Ir^{4+} $4f_{7/2}$, and Ir^{3+} $4f_{7/2}$, respectively. According to the study by Chen et al [14], the amount of Ir used in XPS analysis ranged from 10% to 100% by mol, allowing for XPS detection. Moreover, the study by Christensen et al [22] indicated that after doping Ni into Sb-SnO_2, Ni was incorporated underneath the surface of the material, making it undetectable by surface analysis techniques. This could be another reason why Ir peaks were not observed.

Furthermore, for the $Sn3d_{3/2}$ and $Sn3d_{5/2}$ photoelectron peaks for the Ir/ATO crystals, the binding energies were 495.52 eV and 487.10 eV, respectively. The difference between the $Sn3d_{3/2}$ and $Sn3d_{5/2}$ peaks was 8.4 eV, consistent with the oxidation state of Sn^{4+} [26]. However, in the $Sb3d_{3/2}$ and $Sb3d_{5/2}$ photoelectron peaks in Fig. 7, it was found that the $Sb3d_{5/2}$ peak overlaps the binding energies of both Sb and O. Therefore, the $Sb3d_{3/2}$ peak was employed for analysis. The binding energies for Ir/ATO were 540.07 eV and 540.77 eV, corresponding to the oxidation states of Sb^{3+} and Sb^{5+}, respectively, suggesting an overall Sn^{4+}, Sb^{3+}, and Sb^{5+} [3, 17] oxidation state

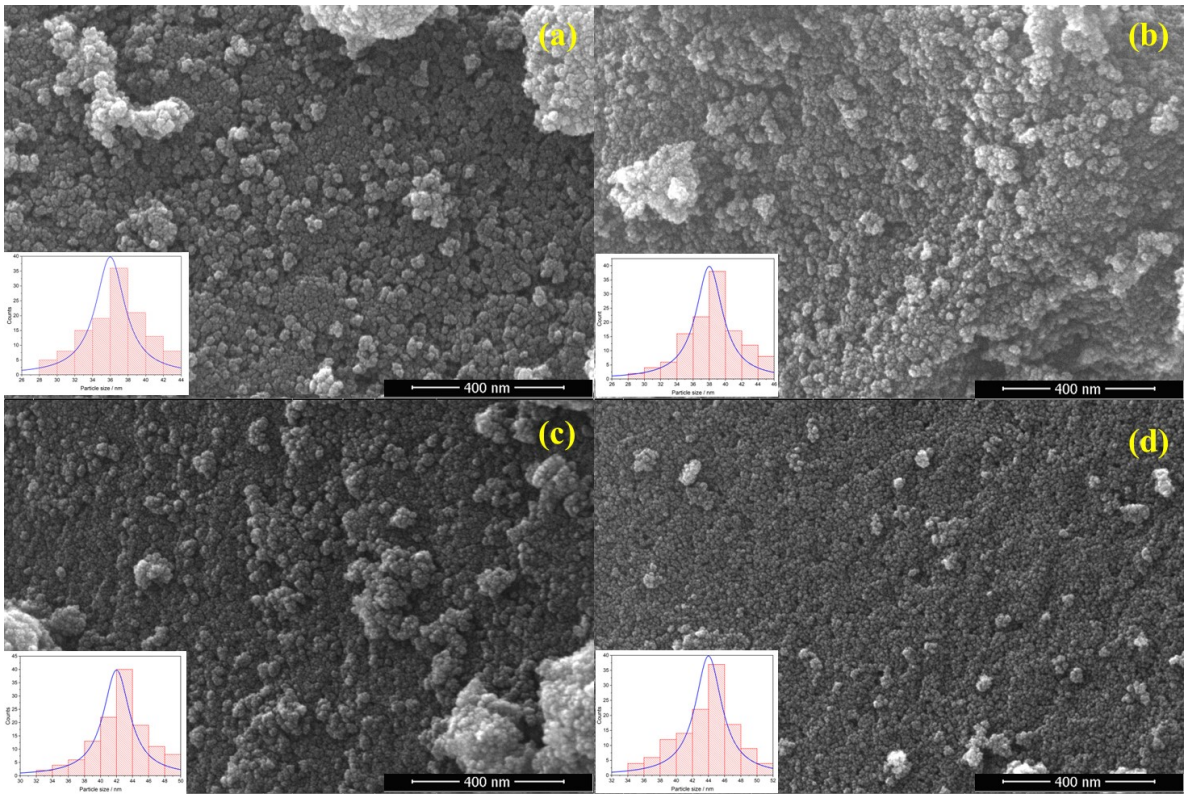

Fig. 4 Typical SEM images along with histograms depicting particle size distribution of Ir/ATO thin film coated on Ti calcined at 550 °C with various Ir contents of (a) 0.5%, (b) 1%, (c) 2%, and (d) 2.5% in the precursor solutions.

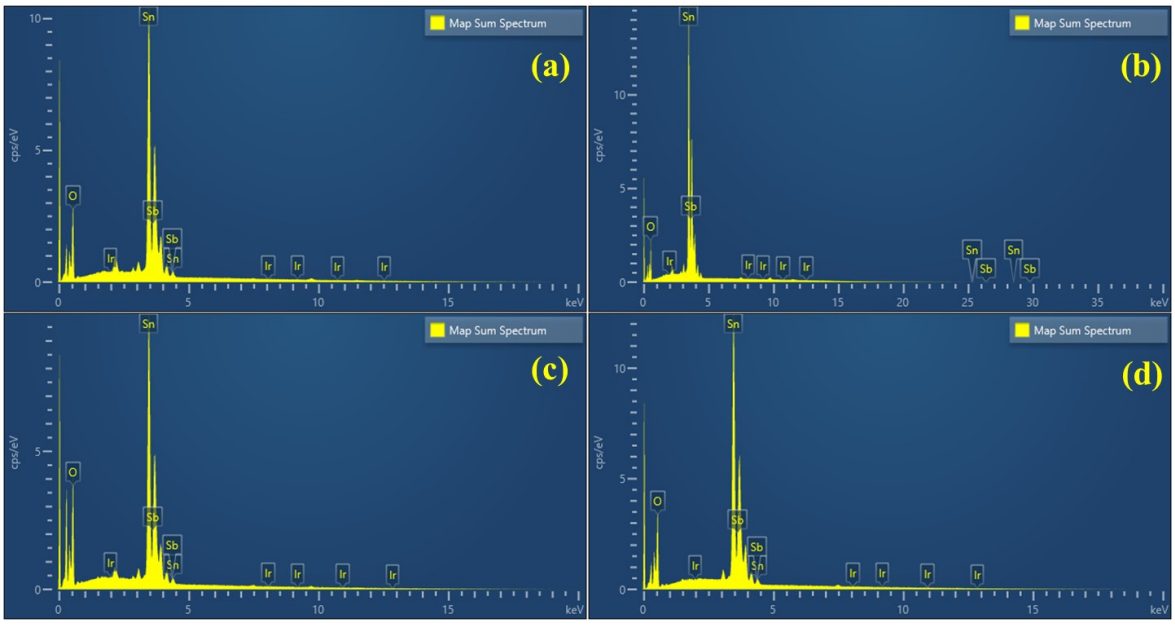

Fig. 5 EDX spectra of Ir/ATO calcined at 550 °C with various Ir contents of (a) 0.5%, (b) 1%, (c) 2%, and (d) 2.5% by mol.

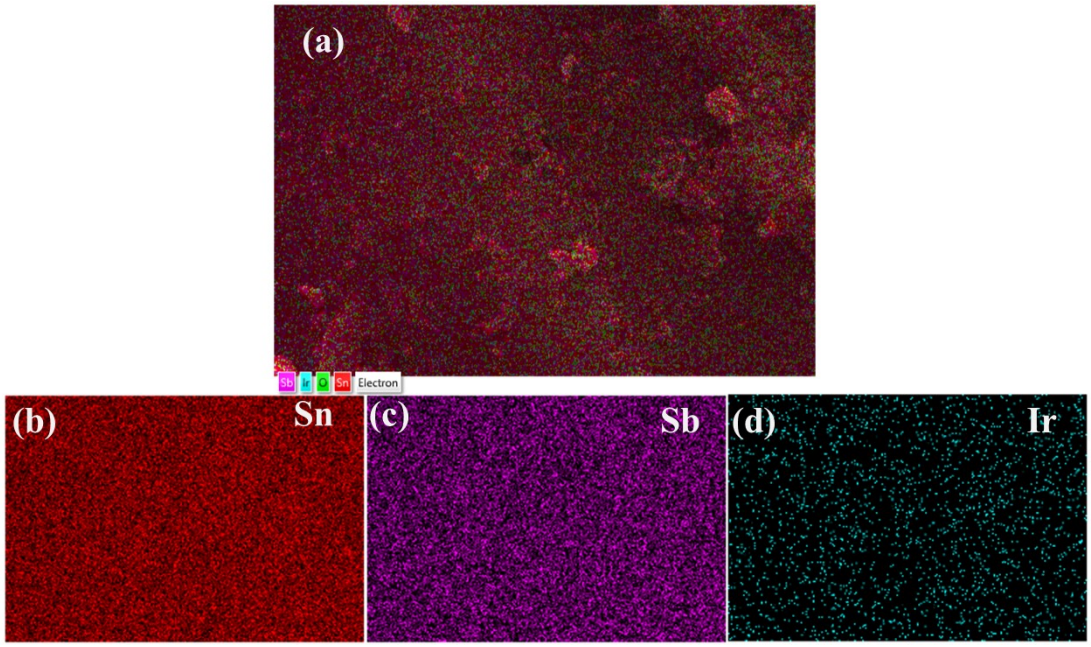

Fig. 6 (a) EDX mapping images of Ir/ATO electrodes calcined at 550 °C with an Ir doping concentration of 2.5% by mol, showing the elemental distribution of (b) Sn, (c) Sb, and (d) Ir.

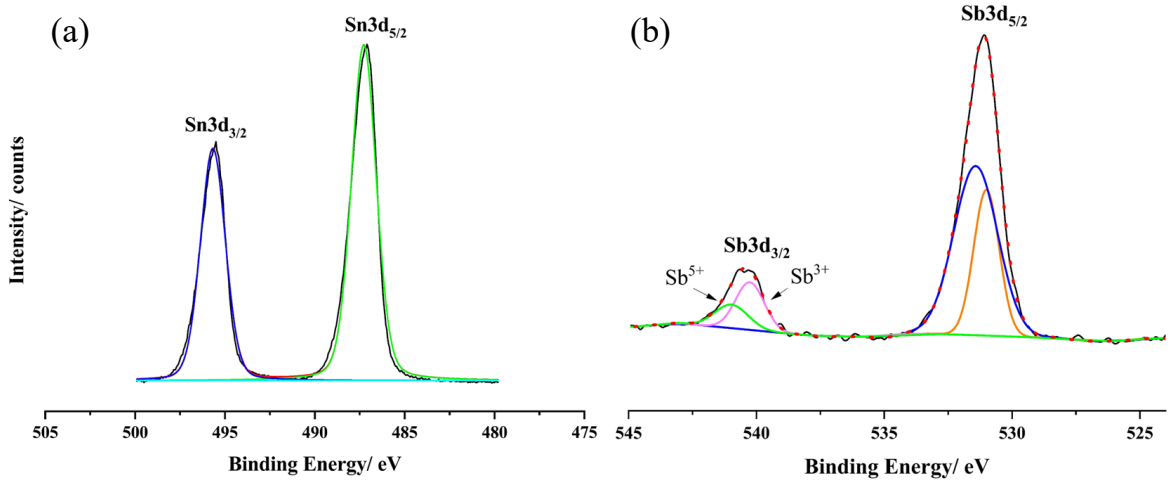

Fig. 7 XPS spectra of (a) Sn and (b) Sb in Ir/ATO catalyst calcined at 550 °C with an Ir doping concentration of 2.5% by mol.

in Ir/ATO catalysts.

With respect to the peak area of the $Sb3d_{3/2}$ in Fig. 7, the area under the Sb^{3+} peak in Ir/ATO increases, indicating an increase in the amount of Sb^{3+} in the Ir/ATO catalyst. This increase in Sb^{3+} could influence the electrical resistance of the material [22], leading to higher adsorption energy and improving the kinetics of the OER reaction [4]. This observation agreed with Duan et al [3], who reported that the O1s peak can be divided into two peaks: one at 530.4 eV, corresponding to lattice oxygen species (OL) integrated into the SnO_2 crystal lattice, and another at 531.4 eV, corresponding to adsorbed hydroxyl oxygen species (Oad), representing hydroxyl/oxygen groups that have been adsorbed. The Oad are indicative of electrocatalytic activities. Traditionally, different mechanisms, such as the adsorbed evolution mechanism (AEM) and the lattice oxygen oxidation mechanism (LOM), are employed to explain OER. The AEM involves the production of oxygen via intermediates such as *O, *OH, and or *OOH, which evolve into O_2 molecules from active sites. However, LOM requires the removal of lattice oxygen atoms from the catalyst

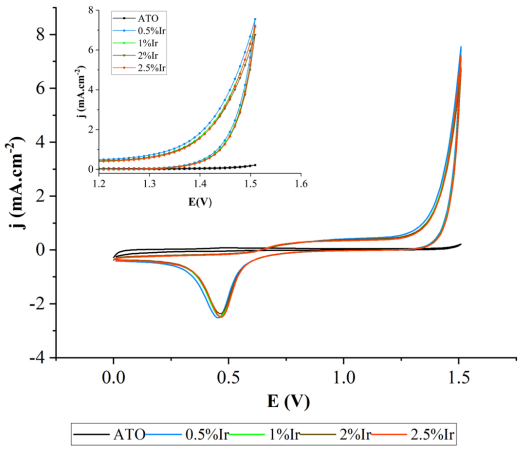

Fig. 8 Cyclic voltammograms of ATO and Ir/ATO with varying Ir concentrations (0.5–2.5 mol%), calcined at 550 °C, measured at 50 mV/s (vs. Ag/AgCl).

to form oxygen vacancies, and this can lead to structural collapse and reduced catalyst durability. Overall, the reaction proceeds via intermediates through active sites, defects, and oxygen vacancies, altering the electron density at the interface. Understanding the behavior of these Oad species is crucial for optimizing the electrocatalytic performance of the catalyst in various applications [22, 27, 28]. Duan et al [3] found that the atomic ratio between Oad and OL was 69.5%, indicating that the electrical activity depends on the value of the Oad. An alternative emerging mechanism called the Oxide Path Mechanism (OPM) is a direct coupling of two adsorbed oxygen atoms or radicals (O—O), leading to the formation of the O_2 molecule [29]. In this study, as the Ir peaks were not observed, the aforementioned increase of the area under the Sb^{3+} peak in Ir/ATO may indicate an alteration in electronic structure. This may be enhanced by the addition of Ir and consequently affect the energy barrier of the O—O bond formation, thereby improving the OER.

Cyclic voltammetry analysis

Fig. 8 shows the CV of ATO and Ir/ATO catalysts with various Ir contents ranging between 0.5% and 2.5% by mol, synthesized at a calcination temperature of 550 °C. As can be seen from the voltammogram, a markedly different profile is observed for ATO compared to Ir/ATO with various Ir doping contents. The CV related to ATO revealed a pseudo-capacitive current response over the investigated voltage window [18, 30]. At 1.5 V, the current density attributed to the OER is around 0.21 mA/cm^2. Unlike ATO, Ir/ATO voltammograms exhibits a reduction peak at approximately 0.47 V (vs. Ag/AgCl), with a current density of 2.03 mA/cm^2 for all investigated doping concentrations. This suggests a change in the properties of Ir/ATO compared to ATO.

Additionally, the onset of surface oxidation at a potential of approximately 0.8 V matches the reported value of 0.93 V for oxidation reactions of iridium metal in various oxide phases in acidic conditions [10]. The graph also indicates redox reactions involving the transitions between Ir^{3+}/Ir^{4+} and Ir^{4+}/Ir^{5+} at 0.68 and 1.2 V, respectively, demonstrating oxidation reactions of iridium or iridium oxide in acidic conditions, depending on the doping concentration. It can be seen that the onset potential for the oxygen evolution reaction (EOER) is approximately 1.45 V and 1.44 V for ATO and Ir/ATO, respectively. However, the onset potential does not vary considerably with Ir content, corresponding to previous studies [4, 10]. Nevertheless, comparing ATO and Ir/ATO, the current density is approximately 35 times higher upon addition of Ir to ATO, emphasizing its superior catalytic activity. The enhanced performance of catalytic activity (i.e., current density) may be due to the introduction of Ir ions. Iridium loading may potentially involve electron transfer between the ATO support and Ir ions, altering the electronic configuration. ATO is an n-type semiconductor capable of producing extra electrons via oxygen vacancies [31, 32]. Introducing Ir may lower the energy barrier, favor charge transfer, and thus boost its electrical conductivity as well as OER, which can be achieved by synthesizing iridium doped ATO through a thermal process [10].

CONCLUSION

The Ir/ATO electrodes were synthesized using the dip-coating method, with Ir doping concentrations ranging from 0.5% to 2.5%, and calcined at a temperature of 450 °C to 550 °C. Ir/ATO anode electrodes have a single tetragonal crystal structure. There is a slight change in the lattice size, as the ionic radii of Sb and Ir can replace that of Sn^{4+}. The XPS investigation revealed that Sn exists in the Sn^{4+} oxidation state, while Sb is present in both Sb^{3+} and Sb^{5+} oxidation states in Ir/ATO. Both Sb^{3+} and Sb^{5+} are key factors contributing to the electrical conductivity of Ir/ATO. Doping Ir into ATO changes its physicochemical properties, with a reduction peak at a potential of approximately 0.47 V (vs. Ag/AgCl) and a current density of 2.03 mA/cm^2 across all doping concentrations. The nanoparticle sizes of Ir/ATO enhance the OER. The onset potential for oxygen evolution reactions is around 1.4 V, with a current density 35 times higher for Ir/ATO compared to ATO.

Acknowledgements: This work was supported by the National Higher Education, Science, Research, and Innovation Policy Council, Thaksin University (Research project grant no. 66A105000010), Fiscal Year 2023.

REFERENCES

1. Cheng Y, Jiang SP (2015) Advances in electrocatalysts for oxygen evolution reaction of water electrolysis-from metal oxides to carbon nanotubes. *Prog Nat Sci Mater Int* **25**, 545–553.
2. Tahir M, Pan L, Idrees F, Zhang X, Wang L, Zou J, Wang L (2017) Electrocatalytic oxygen evolution reaction for energy conversion and storage: A comprehensive review. *Nano Energy* **37**, 136–157.
3. Duan T, Chen Y, Wen Q, Duan Y (2015) Novel composition graded Ti/Ru-Sb-SnO_2 electrode synthesized by selective electrodeposition and its application for electrocatalytic decolorization of dyes. *J Phys Chem C* **119**, 7780–7790.
4. Tong J, Liu Y, Peng Q, Hu W, Wu Q (2017) An efficient Sb-SnO_2-supported IrO_2 electrocatalyst for the oxygen evolution reaction in acidic medium. *J Mater Sci* **52**, 13427–13443.
5. Zhou ZH, Sun W, Zaman WQ, Cao LM, Yang J (2018) Highly active and stable synergistic Ir-IrO_2 electrocatalyst for oxygen evolution reaction. *Chem Eng Commun* **205**, 966–974.
6. Xu J, Li J, Xiong D, Zhang B, Liu Y, Wu KH, Amorim I, Li W (2018) Trends in activity for the oxygen evolution reaction on transition metal (M = Fe, Co, Ni) phosphide pre-catalysts. *Chem Sci* **9**, 3470–3476.
7. Xu W, Lyu F, Bai Y, Gao A, Feng J, Cai Z, Yin Y (2018) Porous cobalt oxide nanoplates enriched with oxygen vacancies for oxygen evolution reaction. *Nano Energy* **43**, 110–116.
8. Gong L, Cheng XYE, Du Y, Xi S, Yeo BS (2018) Enhanced catalysis of the electrochemical oxygen evolution reaction by iron (III) ions adsorbed on amorphous cobalt oxide. *ACS Catal* **8**, 807–814.
9. Marshall AT, Haverkamp RG (2012) Nanoparticles of IrO_2 or Sb-SnO_2 increase the performance of iridium oxide DSA electrodes. *J Mater Sci* **47**, 1135–1141.
10. Pérez-Viramontes NJ, Escalante-García IL, Guzmán-Martínez C, Galván-Valencia M, Durón-Torres SM (2015) Electrochemical study of Ir-Sn-Sb-O materials as catalyst-supports for the oxygen evolution reaction. *J Appl Electrochem* **45**, 1165–1173.
11. Seong KJ, Byunghoon K, Hyunah K, Kisuk K (2018) Recent progress on multimetal oxide catalysts for the oxygen evolution reaction. *Adv Energy Mater* **8**, 1702774.
12. Simon G, Olga K, Mingers MA, Nicley S, Ken H, Mayrhofer KJ, Serhiy C (2017) Catalyst stability benchmarking for the oxygen evolution reaction: The importance of backing electrode material and dissolution in accelerated aging studies. *ChemSusChem* **10**, 4140–4143.
13. Oh H-S, Nong HN, Reier T, Bergmann A, Gliech M, Ferreira de Araújo J, Willinger E, Schlögl R, et al (2016) Electrochemical catalyst-support effects and their stabilizing role for IrO_x nanoparticle catalysts during the oxygen evolution reaction. *J Am Chem Soc* **138**, 12552–12563.
14. Chen X, Chen G, Yue PL (2001) Stable Ti/IrO_x-Sb_2O_5-SnO_2 anode for O_2 evolution with low Ir content. *J Phys Chem B* **105**, 4623–4628.
15. Kim JC, Oh SI, Kang W, Yoo HY, Lee J, Kim DW (2019) Superior anodic oxidation in tailored Sb-doped SnO_2/RuO_2 composite nanofibers for electrochemical water treatment. *J Catal* **374**, 118–126.
16. Xu J, Li Q, Hansen MK, Christensen E, Tomás García AL, Liu G, Wang X, Bjerrum NJ (2012) Antimony doped tin oxides and their composites with tin pyrophosphates as catalyst supports for oxygen evolution reaction in proton exchange membrane water electrolysis. *Int J Hydrogen Energy* **37**, 18629–18640.
17. Abbott DF, Lebedev D, Waltar K, Povia M, Nachtegaal M, Fabbri E, Copéret C, Schmidt TJ (2016) Iridium oxide for the oxygen evolution reaction: Correlation between particle size, morphology, and the surface hydroxo layer from operando XAS. *Chem Mater* **28**, 6591–6604.
18. Ávila-Vázquez V, Cruz J, Galván-Valencia M, Ledesma-García J, Arriaga LG, Guzmán C, Duron-Torres S (2013) Electrochemical study of Sb-doped SnO_2 supports on the oxygen evolution reaction: Effect of synthesis annealing time. *Int J Electrochem Sci* **8**, 10586–10600.
19. Reier T, Oezaslan M, Strasser P (2012) Electrocatalytic oxygen evolution reaction (OER) on Ru, Ir, and Pt catalysts: A comparative study of nanoparticles and bulk materials. *ACS Catal* **2**, 1765–1772.
20. Christensen PA, Attidekou PS, Egdell RG, Maneelok S, Manning DAC (2016) An in situ FTIR spectroscopic and thermogravimetric analysis study of the dehydration and dihydroxylation of SnO_2: The contribution of the (100), (110) and (111) facets. *Phys Chem Chem Phys* **18**, 22990–22998.
21. Maneelok S, Attidekou PS (2023) Electrochemical ozone generation for palm oil mill wastewater treatment using nickel and antimony doped tin oxide anodes. *Suranaree J Sci Technol* **30**, 030100(1-7).
22. Christensen PA, Attidekou PS, Egdell RG, Maneelok S, Manning DAC, Palgrave R (2016) Identification of the mechanism of electrocatalytic ozone generation on Ni/Sb-SnO_2. *J Phys Chem C* **121**, 1188–1199.
23. Kangkamano T, Kongsune P, Suwanraksa K, Charoenlap T, Khaophong S, Intachai S (2025) Effect of temperature of boric acid-doped porous activated carbon preparation on the electrochemical capacitor performance. *ScienceAsia* **51**, ID 2025031.
24. Thungsuai K, Pimpha N, Chaleawlert-umpon S (2023) The role of carbon electrode parameters on capacitive deionization efficiency. *ScienceAsia* **49**, 859–863.
25. Bai N, Qi Y, Miu X, Yin J, Guo D, Wang J, Wang A (2023) Direct blending-drying method of graphitic carbon nitride (g-C3N4) with copper chloride solution for enhancement of photocatalytic decolorization of methylene blue. *ScienceAsia* **49**, 192–199.
26. Yang SY, Choo YS, Kim S, Lim SK, Lee J, Park H (2012) Boosting the electrocatalytic activities of SnO_2 electrodes for remediation of aqueous pollutants by doping with various metals. *Appl Catal B Environ* **111**, 317–325.
27. Zhang G, Chen Q, Liu C, Fan D, Sun Y, Tang H, Sun H, Feng X (2022) Competitive adsorption: Reducing the poisoning effect of adsorbed hydroxyl on Ru single-atom site with SnO_2 for efficient hydrogen evolution. *Angew Chem* **61**, 134–142.
28. Cheng J, Yang J, Kitano S, Juhasz G, Higashi M, Sadakiyo M, Kato K, Yoshioka S, et al (2019) Impact of Ir-valence control and surface nanostructure on oxygen evolution reaction over a highly efficient Ir-TiO_2 nanorod catalyst. *ACS Catal* **9**, 6974–6986.
29. Rong C, Huang X, Arandiyan H, Shao Z, Wang Y, Chen

Y (2025) Advances in oxygen evolution reaction electrocatalysts via direct oxygen-oxygen radical coupling pathway. *Adv Mater* **37**, 2416362–2416382.
30. Lee S-G, Han S-B, Lee W-J, Park K-W (2020) Effect of Sb-doped SnO_2 nanostructures on electrocatalytic performance of a Pt catalyst for methanol oxidation reaction. *Catalysts* **10**, 866–881.
31. Khan IA, Morgen P, Gyergyek S, Sharma R, Andersen SM (2023) Selection on antimony-doped tin oxide (ATO) as an efficient support for iridium-based oxygen evolution reaction (OER) catalyst in acidic media. *Mater Chem Phys* **308**, 128192.
32. Utriainen M, Kovács K, Campbell JM, Niinistö L, Réti F (1999) Controlled electrical conductivity in SnO_2 thin films by oxygen or hydrocarbon assisted atomic layer epitaxy. *J Electrochem Soc* **146**, 189.